PHYSICAL REVIEW FLUIDS **8**, 043301 (2023)

Dynamics of a Newtonian droplet in the turbulent flow of a shear thinning fluid in a microchannel

Yongbin Ji[*]
Department of Mechanical and Automation Engineering, The Chinese University of Hong Kong, 000000 New Territories, Hong Kong SAR, China

Elia Missi,[†] Jérôme Bellettre,[‡] and Teodor Burghelea[§]
LTeN UMR CNRS 6607, Nantes Université, 1 rue Christian Pauc, CS 50609, 44306 Nantes Cedex 3, France

Agnès Montillet[‖]
Nantes Université, Oniris, CNRS, GEPEA, UMR 6144, F-44600 Saint-Nazaire, France

Patrizio Massoli[¶]
Institute of Sciences and Technologies for Sustainable Energy and Mobility (STEMS) - CNR, Viale Marconi 4, 80125 Napoli, Italy

(Received 5 May 2022; accepted 20 March 2023; published 12 April 2023)

A systematic experimental investigation of the dynamics of a Newtonian drop in microscopic cross-slot of a shear thinning and inelastic fluid (aqueous solutions of xanthan) is presented. The flows are driven at large Reynolds numbers and are relevant to efficient high-throughput emulsification in microchannels. Depending on the initial size of the drop, the driving flow rates and the rheological behavior of the continuous phase, two fundamental dynamic modes are observed. The first dynamic mode relates to the trapping of the drop. By time-resolved tracking of both the positions and the deformations of the drop over 100 distinct drops a comprehensive statistical description of the trapping events is provided. The probability of trapping when xanthan solutions are used as a continuous phase follow a common trend when the effective strength of the swirling flow motion within the impingement region is gradually increased by tuning both the flow rates and the polymer concentration, suggesting that the trapping events emerge via an imperfect bifurcation. A second phenomenon that is of particular relevance to the emulsification process relates to the breakup of drops. The dynamics of the breakup process are quantitatively described in terms of the characteristic breakup times, number of emerging daughter droplets, and drop morphology are equally dependent on both the driving flow rates and the polymer concentration. Further physical insights into the intricate coupling between the flow conditions, the shear thinning rheology of the continuous phase, and the single-drop dynamics are obtained in terms of a quantitative description of the kinematics of drop deformation. This analysis was performed using a novel tool that allows one to assess the velocity distributions along the drop contours and extract the rates of deformation, the strains corresponding

---

[*] johong.bin@gmail.com; Department of Mechanical and Automation Engineering, The Chinese University of Hong Kong, 000000 New Territories, Hong Kong SAR, China.

[†] elia.missi@univ-nantes.fr

[‡] jerome.bellettre@univ-nantes.fr

[§] teodor.burghelea@univ-nantes.fr

[‖] agnes.montillet@univ-nantes.fr

[¶] patrizio.massoli@stems.cnr.it

to the breakup process, and the kinematic print of the flow (shear or extension). Finally, a full diagram mapping all the modes of the single-droplet dynamics is presented.

DOI: 10.1103/PhysRevFluids.8.043301

I. INTRODUCTION

Understanding the physics of deformation of interfaces between immiscible fluids is of paramount importance for a number of modern day industrial sectors including (but not limited to) pharmaceutic, cosmetics, food, polymer processing, and oil field engineering. The emulsification understood as the physical process that transforms an equilibrium system of two immiscible fluids initially separated by a geometrically simple interface into a system consisting of a collection of drops of one fluid suspended in the second is of particular practical interest. The emulsification is typically obtained via a sequence of out-of-equilibrium processes that lead to the successive deformation and ultimate the breakup of the initial interface. From a thermodynamic standpoint, the progressive increase in the complexity of the initial interface associated with the emulsification process relates to a drastic increase of the entropy of the system. In isothermal conditions, such entropy increase is solely possible when external mechanical work is supplied to the system [1,2]. In the case of a two-phase fluid system initially at equilibrium this work is supplied in the form of flow which drives it far away from equilibrium. Environmental considerations including the energy transition which is nowadays an official policy of the European Union call for the use of bio-based fluids as input for the emulsification process (such as biopolymers) [3]. Nearly all such environmentally friendly fluids are non-Newtonian, which adds a distinct layer of complexity to the emulsification problem because they are characterized by a nonlinear stress-rate of deformation relationship [4].

Depending on the practical context, the emulsification applications may be sorted into two broad classes. The first class relates to what is generally referred to in the literature as "*drop on demand*" protocols. Thus, when small amounts of emulsions with finely tuned properties (size, dispersity, chemical content) are sought in applications related, for example, to precise chemical synthesis, encapsulation there exist a number of microfluidic solutions that operate at low throughput (typically smaller than mL/h) in a creeping flow regime i.e., at very low Reynolds numbers ($Re < 0.1$) [5].

While the dynamics of the drop formation in low Reynolds microscopic flows of Newtonian fluids is relatively well understood, the case of non-Newtonian still makes the object of current studies. The bulk of studies involving non-Newtonian fluids relates to viscoelastic fluids. Guido and coworkers investigated the deformation of a single drop in a dilute polymer blend for slow steady shear flow by microscopy and image analysis [6]. They conclude that the drop orientation in the shear flow is strongly enhanced due to normal stresses of the matrix fluid.

Tretheway and Leal studied experimentally the deformation and relaxation of a Newtonian suspended extensional flow of a Boger fluid [7]. For steady extensional flows, the stronger the viscoelasticity of the matrix fluid is, the larger the drop deformation becomes.

The viscoelastic behavior of the continuous phase also influences the breakup dynamics of Newtonian liquid bridges. Derzsi and coworkers studied experimentally the dynamics of a Newtonian liquid stream and the droplet generation in the microfluidic flow focusing device in a viscoelastic continuous phase [8]. They found that the operation regimes in the flow focusing system (dripping without satellites, dripping with single satellites, multiple satellites, and jetting) are similar for both Newtonian and non-Newtonian fluids. However, the viscoelasticity tends to stabilize the jets producing relatively smaller droplets by carefully adjusting the viscosity ratio. Nooranidoost and coworkers have studied the effect of bulk fluid viscoelasticity on droplet formation and dynamics in the flow focusing configuration using a numerical method and concluded that the viscoelasticity has a similar effect as decreasing the flow rate ratio and thus acts to delay the transition from different regimes [9].

Along with the viscoelasticity [10], the shear-thinning behavior is important to many industrial applications involving microfluidic droplet fabrication. Ren and coworkers have characterized the breakup dynamics and dripping-to-jetting transitions under various flow conditions in a Newtonian or shear-thinning multiphase flow focusing microsystem via both experimentation and numerical simulation [11]. For shear-thinning fluids, they show that the droplet size increases when the capillary number is smaller than a critical value, while it decreases when the capillary number is beyond the critical value.

Fragkopoulos and coworkers presented an experimental investigation of the breakup dynamics of toroidal droplets of a Newtonian liquid in a shear thinning continuous phase [12]. They pointed out that the droplets resist to breakup for times that are longer than those in the linear-behavior Newtonian liquids. By incorporating the nonlinearities of the strain-rate-dependent viscosity correlation, they scaled the growth rate with the shear strain rate in the breakup point, illustrating that both the viscoelastic and shear-thinning nature of the outside material play a crucial role in the drop dynamics.

The dynamics of slender drop formation using in a microscopic flow focusing device was studied by Fu and coworkers [13]. Their results indicate that the minimum width of the dispersed thread scales as a power-law with the time for both Newtonian and shear-thinning continuous phases, but with totally different parameters. A similar conclusion was reached by Zhou and coworkers in different type of microfluidic device, a T-junction configuration [14]. Chiarello and coworkers have also investigated the effect of the shear-thinning rheology on droplet formation in the T-type microchannel [15]. They show that the final emulsion drop size may be accurately predicted by knowing the rheology of the bulk continuous phase in advance [16].

More recently, Agarwal *et al.* performed a parametric numerical study of the process of droplet formation in a T-junction microchannel with a shear-thinning continuous phase [17]. Using the Carreau-Yasuda model to model the shear-thinning behavior, they found that higher shear-thinning tends to produce larger droplets with a plug-like shape instead of the spherical one typically observed in the Newtonian case.

The studies concerning drop dynamics within a shear-thinning matrix briefly reviewed above relate to small flow throughput (of the order of mL/h) applications or laminar flows. There exist, however, certain practical applications where one continuously produces emulsions at high throughput using non-Newtonian fluids.

A recent experimental study has investigated the possibility of making such emulsions at flow rates up to 600 mL/min [18]. A systematic study of the dynamics of the emulsification process at high throughput (or Reynolds number) and in the presence of shear-thinning rheological behavior poses a number of formidable theoretical challenges related to the presence of two sources of nonlinearity: inertial (related to the large values of the Reynolds number) and rheological (related to the nonlinear stress-strain dependence). A systematic experimental study of the high Reynolds number emulsification in the presence of the shear-thinning matrix is an equally daunting task because it requires simultaneous measurements of the dynamics of multiple drops and of the flow fields within the continuous phase.

Here we focus on a presumably simpler physical setting consisting of a Newtonian drop that evolves within the turbulent microscopic flow of a shear-thinning fluid. The shear-thinning rheological behavior is often accompanied by viscoelastic effects. To study solely the role of shear thinning on the single droplet dynamics we focus through this study on fluids that exhibit a strong shear-thinning behavior but no significant elasticity. Through the experiments reported herein two coupled sources of nonlinearity are expected to influence the dynamics of a single drop. The first one is of a rheological nature and relates to the shear-thinning behavior of the continuous phase. This should not be confused with the elastic nonlinearity which typically manifests in the presence of strong viscoelastic effects [4]. The second source of nonlinearity relates to inertial effects which are predominant during turbulent flows.

Several fundamental aspects in relation to both the rheology of the continuous phase and the flow conditions are investigated: statistics of drop shapes, statistics of drop breakup events, morphology of the disperses phase fragmented upon the primary breakup of a drop, and kinematics of the drop-breakup process.

The paper is organized as follows: The experimental methods are described in Sec. II. The choice and rheological properties of the xanthan are briefly described in Sec. II A. The experimental setup, the instrumentation, the data-acquisition protocol, and the data analysis procedure are detailed in Sec. II B. The experimental results are presented in Sec. III, which is structured according to the two main physical phenomena that the present contribution aims to understand. The dynamics of trapping of individual Newtonian drops within the cross-slot flow are systematically analyzed in Sec. III B. The breakup dynamics of single oil drops are described in Sec. III C. The paper closes with a concise summary of the main findings and a discussion of some perspectives in Sec. IV.

II. EXPERIMENTAL METHODS

A. Choice and rheological characterization of the working fluids

1. Choice of working fluids

As a continuous study we have used aqueous solutions of xanthan gum. The xanthan gum is a biopolymer produced by a soil bacterium "*Xanthomonas campestris*" and is one of the most popular hydrocolloids used in various industrial sectors (cosmetics, pharmaceuticals, energy, enhanced oil recovery) applications. This gum is an anionic hetero-polysaccharide consisting of a linear cellulose skeleton of β-D-glucoses of which every second unit is substituted in C_3 by a trisaccharide side chain. Xanthan gum solutions are known to present a significant shear-thinning behavior that becomes more pronounced as the polymer concentration is gradually increased [19] but no elasticity. More specifically, several concentration regimes can be encountered according to the polysaccharide concentration used [20]. The "*dilute regime*" is characterized by small or no steric effects, which translates into a weakly-shear-thinning behavior [21]. Beyond a critical concentration, denoted as C^*, physical interaction gets significant between molecules [22]. The corresponding regime is coined as the "*semidilute regime*." However, internal forces are still dominated by the interactions between the solvent and the polymer [23]. A second critical concentration value C^{**} defines a limit beyond which the system is in the "*concentrated regime*" in the sense that the polymer molecules become entangled. Above the overlap concentration the viscosity increases significantly with the polymer concentration, and a pronounced shear-thinning behavior is observed [21].

The experiments reported herein were performed with a commercial xanthan gum purchased in an anhydrous form (Keltrol$^{\mathrm{TM}}$ *AP* from Kelco) and dissolved in tap water. The powder was added gradually to the solvent at ambient temperature in a mixing vessel under agitation, using a stirrer. The mixing and dissolution process was carried on for 4 hours in order to achieve complete dissolution and homogenization. The xanthan solutions used through this study were formulated at four different concentrations [0.05% (wt), 0.1% (wt), 0.15% (wt), and 0.2% (wt)]. It is difficult to find universal values for bounds of the three concentration regimes C^* and C^{**} based on the literature survey described above. This is mainly due to the physico-chemical variety of xanthan gums used by various authors and to the various methodologies applied. However, the range of concentrations tested through this study is mostly consistent with the dilute regime and possibly with the semidilute regime for the highest tested concentration used. No preservative or surfactant was used in the formulation.

The addition of polymers is often associated with changes in the interfacial tension. For the xanthan solutions and the oil used in this study, however, no significant dependence of the interfacial tension σ_i was found. In the range of xanthan concentrations explored the average interfacial tension was found $\sigma_i = 21.5(\pm 0.3)$ mN/m while the interfacial tension between oil and pure water was 21.8 mN/m.

Dilute raw emulsions [5% (v/v)] were obtained by stirring a commercial rape-seed oil into one of the respectively tested continuous phase. The diameters of the oil drops are broadly distributed following a log-normal distribution in between $D_{\min} = 100$ µm and $D_{\max} = 200$ µm.

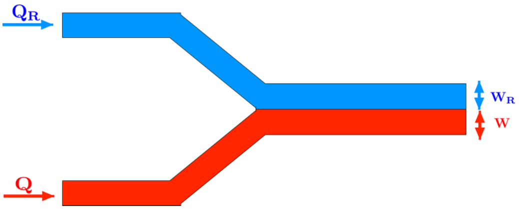

FIG. 1. Schematic representation of the high shear rate microfluidic rheometer: Q is the flow rate of the fluid to be characterized, Q_R is the flow rate of the reference fluid with a known viscosity, W is the transverse extent of the fluid to be characterized, and W_R is the transverse extent of the reference fluid.

2. *Rheological characterisation of the fluids*

The rheological behavior of aqueous solutions of xanthan gum is well described by the Carreau-Yasuda model. Within this framework the shear viscosity η is related to the rate of shear $\dot{\gamma}$ via

$$\eta = \eta_\infty + (\eta_0 - \eta_\infty)[1 + (\lambda\dot{\gamma})^2]^{(n-1)/2}. \tag{1}$$

Here $\eta_0 = \lim_{\dot{\gamma}\to 0} \eta(\dot{\gamma})$ stands for the zero shear viscosity, $\eta_\infty = \lim_{\dot{\gamma}\to\infty} \eta(\dot{\gamma})$ for the infinite shear viscosity, λ sets a scale $(1/\lambda)$ for the shear rate marking the onset of the shear-thinning behavior, and $n \in [0, 1]$ is the power-law index that characterizes the steepness of the shear-thinning behavior observed between the two viscosity plateaus.

As the drop dynamics experiments have been performed at high flow rates in an inertially turbulent regime, it was important to characterize the rheological behavior of the xanthan solutions used in this study in a broad range of shear rates, $\dot{\gamma} \in [1\ \mathrm{s}^{-1}\text{–}10^5\ \mathrm{s}^{-1}]$. It is equally important to note that, as the infinite shear viscosity plateau is typically observed at large rates of shear, an accurate fit by the Carreau-Yasuda model equally requires varying the shear rates over the broad range mentioned above.

To cover this particularly broad range of shear rates relevant to our study of drop dynamics we have combined conventional rotational rheometry with high shear rate rheometry on a chip [24].

The high shear rate rheological tests have been performed using a microfluidic rheometer (FLUIDICAM RHEO$^{\mathrm{TM}}$ from Formulaction, France) which allows one to probe a broad range of shear rates, $\dot{\gamma} \in [3000\ \mathrm{s}^{-1}, 2 \times 10^5\ \mathrm{s}^{-1}]$. A detailed description of the operating principle of this device can be found in Ref. [25]. The fluid to be characterized is injected side by side with a reference fluid (with a known viscosity) in a Y-shaped microchannel with a width $W_{total} = W + W_R = 2200\ \mu\mathrm{m}$, as schematically illustrated in Fig. 1. Using successively two microchips with channels of different heights, $h = 50$ and $150\ \mu\mathrm{m}$ allows us to cover the above-cited range of shear rates.

The flow rates Q_R, Q of the reference fluid and of the fluid to be characterized are precisely controlled using two accurate microsyringe pumps. As a reference Newtonian fluid, a solution of polyethylene glycol (PEG) with a viscosity of $\eta_R = 6.85$ mPa s at $T = 25\,^\circ\mathrm{C}$.

Due to the small size of the channel the flows are laminar and fully developed at the channel outlet. Thus, the ratio of the transverse extents of the two fluids W/W_R near the outlet of the microfluidic device is proportional to the ratio of the apparent viscosity η_{app} of the fluid to be characterized and the known viscosity η_R of the reference fluid [26,27]:

$$\frac{W}{W_R} = \frac{\eta_{\mathrm{app}}}{\eta_R}\frac{Q}{Q_R}. \tag{2}$$

Thus, according to the simple relationship above, monitoring optically the ratio W/W_R and knowing the flow rates Q, Q_R allows one to extract the ratio $\frac{\eta_{\mathrm{app}}}{\eta_R}$ between the apparent viscosity of the fluid to be characterized to the known viscosity of the reference fluid. The ratio W/W_R is

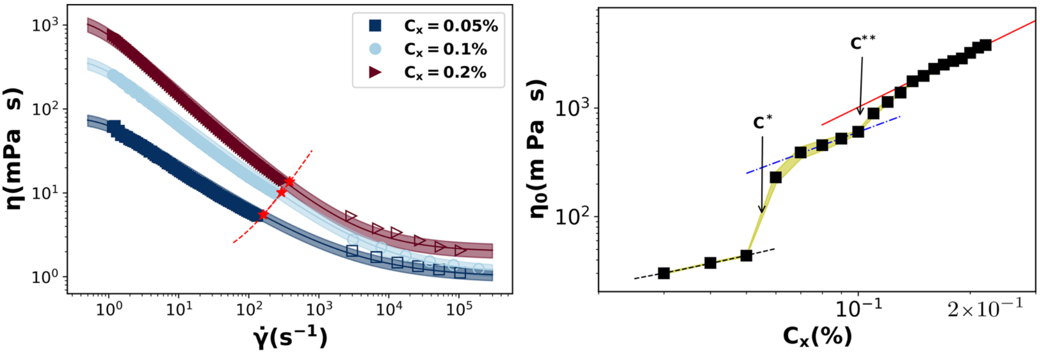

(a) (b)

FIG. 2. (a) Rheological flow curves measured for three distinct xanthan concentrations indicated in the inset via two alternative techniques (see text for description) classical rotational rheology (full symbols), microfluidic high shear rate rheology (open symbols). The full lines are nonlinear fitting functions obtained according to the Carreau-Yasuda model and the highlighted regions indicate the confidence interval of the fitting procedure. The stars and the dashed line mark the critical line $(\dot{\gamma}_c, \eta_c)$ defined by the condition $Re_c = 0.1$ that defines the inertia-free range of the classical rotational rheology measurements (see text for details and discussion). (b) Dependence of the zero shear viscosity η_0 on the concentration of xanthan C_x. The lines are power-law fitting functions (see text for description). The vertical arrows point the concentration bounds C^*, C^{**} of the relevant concentrated regimes.

accurately measured by acquiring a time series of images of the interface between the two fluids and subsequent image processing.

The true rate of shear experienced by the fluid to be characterized may be expressed according to Weissenberg-Rabinowitsch-Mooney equation [28]:

$$\dot{\gamma}_{\text{true}} = \frac{\dot{\gamma}_{\text{app}}}{3}\left[2 + \frac{d\ln\dot{\gamma}_{\text{app}}}{d\ln\tau}\right], \tag{3}$$

where $\dot{\gamma}_{\text{app}} = 6Q/(Wh)$, h is the height of the microchannel [29] and $\tau = \dot{\gamma}_{\text{true}}\eta = \dot{\gamma}_{\text{app}}\eta_{\text{app}}$ is the true stress imposed onto the tested fluid. High shear rate viscosities are shown in Fig. 2(a) as empty symbols.

The classical rotational rheometry tests were performed using a Mars III (Thermofischer Scientific) device which is a controlled stress rotational rheometer equipped with a nanotorque module. Tests were performed using a cone and plate geometry with a radius $R = 30$ mm and a truncation angle $\alpha = 2^\circ$ (for HAAKE MARS). The temperature was regulated at $25 \pm 0.05\,^\circ$C using both a Peltier system embedded in the bottom plate of the rheometer and an electrical oven enclosure mounted on the top of the geometry. The number of steps for each branch of the ramp was $N = 100$ and the averaging time per step was 30 s. Measurements have been performed by imposing increasing or decreasing controlled shear rate ramps ranging from 1 s^{-1} to a maximal shear rate $\dot{\gamma}_c$ beyond which inertial instabilities are expected to occur within the cone-plate flow. Such rotational measurements are shown as full symbols in Fig. 2(a).

The critical shear rate $\dot{\gamma}_c$ corresponds to a critical value of Reynolds number Re_c above which the cone-plate flow turns inertially unstable (and thus it is no longer a rheometric flow). As we are not aware of any analytical result predicting the value of Re_c for a cone-plate geometry for a shear-thinning fluid, we have (rather arbitrarily) chosen $Re_c = 0.1$. However, the determination of the critical shear rates $\dot{\gamma}_c$ corresponding to the onset of the inertial (nonrheometric) flow regime is not straightforward which calls for a detailed description. First, high shear rate viscosity data has been obtained according to the procedure detailed above. Next, we have retained only the rotational rheological data corresponding to $\dot{\gamma} < 100\ \text{s}^{-1}$ and performed a first rough nonlinear fit of these data combined with the high shear rheometry data according to the Carreau-Yasuda model, Eq. (1). This rough nonlinear fit allows one to compute the Reynolds numbers corresponding to the rotational measurements according to

$$Re = \frac{\rho (R \tan \alpha)^2 \dot{\gamma}}{\eta_\infty + (\eta_0 - \eta_\infty)[1 + (\lambda \dot{\gamma})^2]^{(n-1)/2}}, \tag{4}$$

where ρ is the density of the xanthan solution. Next, the maximal values of shear rates $\dot{\gamma}_c$ have been computed using Eq. (4) and the condition $Re(\dot{\gamma}_c) = 0.1$.

We illustrate combined measurements of the shear viscosity performed for three distinct concentrations of xanthan in Fig. 2(a).

A nonlinear fit based on the Levenberg-Marquardt algorithm according to the Carreau-Yasuda model has been performed on the rotational data corresponding to $\dot{\gamma} < \dot{\gamma}_c$ and to the high shear rate data—see the full lines in Fig. 2(a). The confidence bounds of the nonlinear fitting functions shown as highlighted regions account for roughly 15%–20% of the measured value of the viscosity. The bounds of the inertial regime are marked with stars in Fig. 2(a).

To identify various concentration regimes relevant to the drop dynamics experiments reported herein, we illustrate in Fig. 2(b) measurements of the zero shear viscosity performed in a range of xanthan concentrations C_x relevant to our experiments. For low concentrations of xanthan, $C_x \leqslant 0.05\%$, the zero shear viscosity increases linearly with the xanthan concentration [see dashed line in Fig. 2(b)], which is what one would expect for a dilute concentration regime. Past a critical value of the xanthan concentration $C^* \approx 0.05\%$ a power-law scaling of the zero shear viscosity with the xanthan concentration is observed, $\eta_0 \propto C_x^{1.26\pm0.12}$. We identify this range of concentrations with the so-called "*semidilute regime*". Increasing the xanthan concentration even further past $C^{**} \approx 0.1\%$ a third scaling regime is observed $\eta_0 \propto C_x^{1.67\pm0.15}$. This corresponds to the so-called "*concentrated regime*".

To our best knowledge, data on the scaling of the zero shear viscosity with the xanthan concentration are rather scarce in the literature. We compare in the following our scaling results with those obtained by Nsengiyumvaa and Alexandridisa [30]. As a polymer, they have used Keltrol T 622, Mat. #20000625 by CP Kelco (while we used a slightly different grade, Keltrol AP). The scaling behavior they found within the semidilute regime is very different than ours ($\eta_0 \propto c^{0.5}$ while we found $\eta_0 \propto c^{1.2}$). On the other hand, the scaling behavior they found in the concentrated regime is closer to ours ($\eta_0 \propto c^{1.5}$ while we found $\eta_0 \propto c^{1.67}$). We attribute these discrepancies to several factors: differences in the grade of xanthan, differences in the salt content of the solutions (our solutions were prepared in tap water so their ionic content was not controlled) and possible differences in the rheometric procedure.

The bulk of the droplet dynamics experiments reported herein correspond the semidilute and concentrated concentration regimes.

B. Experimental setup

1. Microscopic flow channel

The experiments have been conducted in a cross-slot microchannel as schematically illustrated in Fig. 3. The microchannel was machined from an acrylic block with the dimensions 70 mm × 40 mm × 18 mm using a fast-spinning (14 000 rev/min) micromilling head (Nakanishi, model $HES510$-$BT40$) mounted on a commercial computer controlled milling machine (Twinhorn, model $VH1010$). This micromilling technique has been previously used in microfluidics [31,32].

By a precise alignment of the initial acrylic block on the stage of the milling machine, the depths of the microchannel was accurately controlled over its entire length with an end to end variation smaller than one percent. The average roughness of the edges of the microchannel as resulted from the micromilling process is roughly of the order of a micron which accounts for less than a percent of the channel width. The edge smoothness obtained with this micromachining technique is comparable to that obtained via the classical microlithography techniques used to

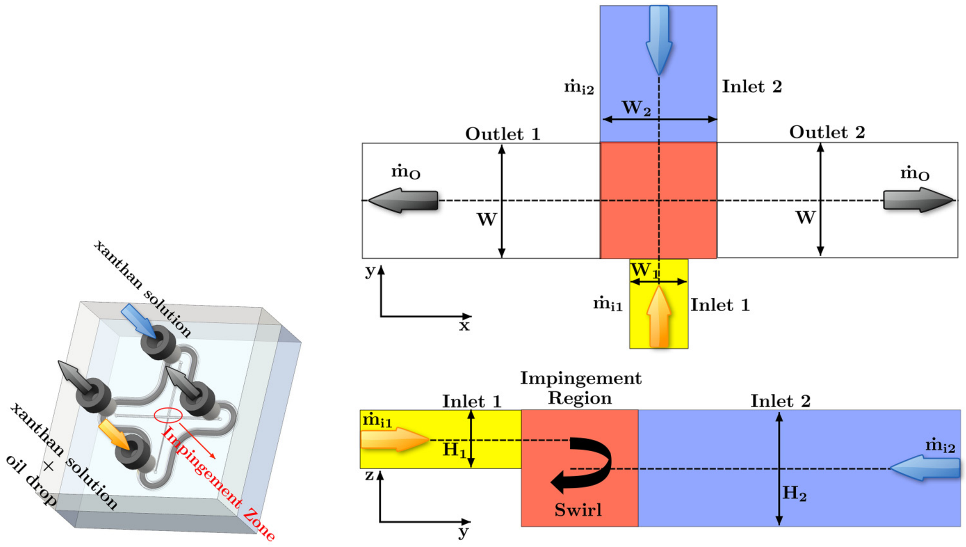

(a) (b)

FIG. 3. (a) Schematic view of the microfluidic chip. (b) Top shows frontal (camera) view of the cross-slot region in the (x, y) plane. Bottom shows lateral view (not accessible through our measurements but only hinted as) of the cross-slot region in the (y, z) plane. Blue and yellow regions refer to the channel inlets while the red highlighted region is the impingement zone. The "*cartoon*" arrow is solely a visual hint for the three-dimensional flow structure dominated by the presence of a swirl located at the center of the cross-slot region later referred to in the paper.

produce polydimethylsiloxane (PDMS) microchannels [33]. However, unlike the more popular polydimethylsiloxane microchannels, the micromilled microchannels are able to sustain very large pressure up to 90 bars, which is essential for performing experiments at very high volumetric flow rates. The microchannel is closed by a second acrylic block fitted with O-rings to prevent fluid leakage via a set of stainless-steel bolts, Fig. 3(a).

The geometry of the microchannel is detailed in Fig. 3(b). This cross-slot geometry has been proposed and studied by Belkadi and coworkers for the case of Newtonian fluids [34]. The solution carrying the single oil drop, i.e., dilute raw emulsion, is fed through an inlet with a rectangular cross-section $H_1 = W_1 = 300$ μm at a mass flow rate $\dot{m}_{i1}$ while a droplet free stream of xanthan solution is fed through an opposite inlet with dimensions twice larger $H_2 = W_2 = 600$ μm at a mass flow rate $\dot{m}_{i2}$, top panel of Fig. 3(b). The uneven dimensions of the two fluid inlets have been purposely chosen in order to generate a swirling flow motion at the impact between the two fluid streams depicted in the cartoon illustrated in the bottom panel of Fig. 3(b). This swirling motion promotes the transition to turbulent flow states which plays a crucial role in the breakup dynamics of the single oil drop.

After impacting within the impingement region highlighted by the red squares shown in Fig. 3(b) the fluids are discharged through two identical outlets. The two channel outlets have a rectangular cross section, $H = W = 600$ μm. The flow rates of the discharged fluids are found to be equal (within 1%). The mean velocity at the outlets U_o is obtained by measuring the outlet flow rates $\dot{m}_{o1} = \dot{m}_{o2} = \dot{m}_o$ [34,35]. Various experiments are referred to by specifying the pair of the volumetric flow rates of the inlet fluids Q_{i_2}-Q_{i_2}.

2. *Data-acquisition system*

The flow control and data-acquisition system are schematically illustrated in Fig. 4. The two fluids injected through the inlets of the microchannel are held in the fluid containers $\mathrm{IFC}_{1,2}$. The

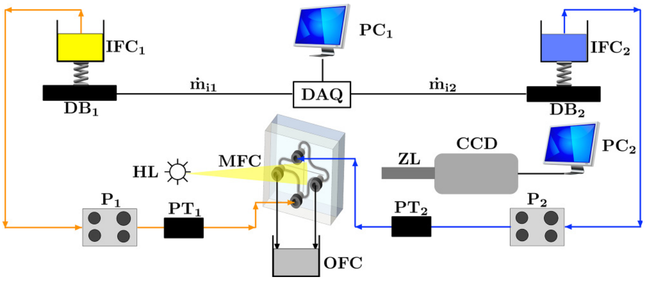

FIG. 4. Schematic representation of the experimental system for the visualization of single drop dynamics: IFC$_{1,2}$: input fluid containers, OFC: output fluid container, DB$_{1,2}$: digital balances, P$_{1,2}$: fluid pumps, PT$_{1,2}$: pressure transducers, PC$_{1,2}$: data-acquisition computers, MFC: microfluidic chip, HL: halogen lamp, CCD: digital camera, ZL: zoom lens.

two inlet fluid containers are mounted on two identical digital balances DB$_{1,2}$ (Sartorius-MSE 2203) which, connected to a personal computer PC$_1$, provide a real time measurements of the flow rates $\dot{m}_{i1,i2}$. The inlet fluids are pumped into the microchannel chip MFC by two pumps P$_{1,2}$ (*AP TRIX* 500 from Armen, France). The fluids collected through the two outlets of the microchannel are discharged in an outlet fluid container OFC. The microchannel is illuminated from behind by a 50 W halogen lamp HL with its optical axis normally aligned to the center of the impingement region of the microchannel. The impingement region is visualized by a fast camera CCD (FASTCAME SA-X2 1080K M$_4$ from Photron) equipped with a 12× magnification zoom lens ZL (Lavision) and connected to a second personal computer PC$_2$. The fast camera is equipped with an image intensifier and can be operated up to the nominal frame rate of 1080 kfps. For the bulk of the experiments reported herein the camera has been operated at 300 kfps and, occasionally, at 150 kfps. To maximize the signal-to-noise ratio of the images, a maximum exposure time of $1/583\,784$ s has been set.

C. Data analysis

The main data analysis tool relates to the processing of individual flow images which allows one to extract the contour of each object (mother or daughter droplets) from each image.

For this purpose, a dedicated image processing package has been developed in-house using the SCIKIT-image module of Python [36]. Several image analysis steps are illustrated in Fig. 5.

The main steps of the image processing sequence are illustrated in Fig. 5(a). The first step consists of computing an average background of 3000 individual flow images similar to the one illustrated in Fig. 5(a). Next, the background is subtracted from each image of the sequence and the contrast of the resulting image is enhanced using an adaptive histogram equalization technique, Fig. 5(b). Note that, after the subtraction of the background, some features visible in Fig. 5(a) and related to impurities present on the channel walls are no longer visible and solely the details of the drops are retained. A binary closure of the enhanced image is performed and individual objects (mother droplet and/or daughter droplets) are detected in each flow image, Fig. 5(c). Finally, the contours and centroids of each object detected in each of the images of the sequence are saved in a text file together with the corresponding time stamp.

This output text file will later serve for assessing several physical quantities relevant to the dynamics of a single drop in the turbulent cross-slot flow which will be detailed later through the paper.

We chose to detail here only one particular processing step we have implemented in order to quantitatively assess the flow kinematics during the dynamics of the droplet. To assess the kinematics of the droplet deformation process, one needs to obtain information of the flow field around it. Such information is typically obtained by means of microscopic particle image velocimetry

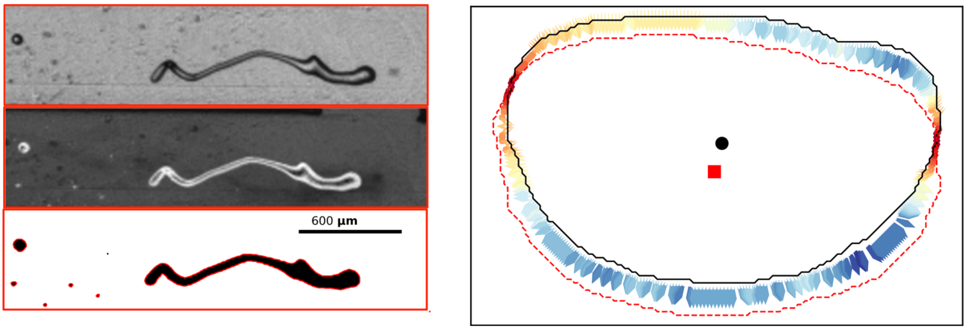

(a) (b)

FIG. 5. (a) Illustrations of the image processing sequence: Top panel shows original image, middle panel shows image after subtracting the background and enhancing the contrast, bottom panel shows binary closed image with the contours of the identified objects (droplets) superposed. (b) Illustration of the front tracking for a mother droplet in a water matrix and the flow rates 50–6.3 mL/min. The black full line represents the initial contour of the drop, the dashed red its final contour. The black circle is the initial centroid of the drop while the red square is its final centroid. The color map of the velocity vectors relates to their magnitude (red shows small values, blue shows large values).

(micro-PIV). Micro-PIV measurements require seeding the matrix fluid with submicron tracers and insuring an illumination of the flow that is generally inconsistent with the white light visualization of drops. Additionally, the light scattered by the flow tracers is proportional to their cubic radius and the frame rate of the image acquisition process is very large (adapted to the large volumetric flow rates of interest). Thus, one needs extremely powerful light sources that are technically problematic to use without overheating the flow channel during the data-acquisition process.

Here we propose an alternative and simple technique that renders the distribution of the velocity along the drop contour in the (x, y) plane which in turn may provide useful information on the flow kinematics. The technique relies on the detection of the drop contour from each frame and is implemented following the steps described below.

The key step of such measurements is to obtain the distribution of the velocity along the contour of the deforming mother drop by a particle tracking algorithm developed in-house that tracks the displacement of each point of the drop contour between successive frames. We illustrate this front tracking procedure in Fig. 5(b).

Considering the velocity gradient tensor $\nabla\mathbf{U}$ where $\mathbf{U} = (u_x, u_y)$ is the two-dimensional vector field measured along the contour of the deforming mother droplet, the strain rate tensor is defined as $\mathbf{D} = \nabla\mathbf{U} + \nabla^{\mathrm{T}}\mathbf{U}$. The global deformation rate of the mother drop is quantified by the second invariant of the strain-rate tensor:

$$D_2 = (2\mathbf{D} : \mathbf{D})^{1/2} = \left\{ 2\left[\left(\frac{\partial u_x}{\partial x}\right)^2 + \frac{1}{2}\left(\frac{\partial u_x}{\partial y} + \frac{\partial u_y}{\partial x}\right)^2 + \left(\frac{\partial u_y}{\partial y}\right)^2 \right] \right\}^{1/2}. \tag{5}$$

The turbulent flow field in the impingement flow region is a rather complex mixture of shear, pure strain (extension), and rigid body rotation.

While the rigid body rotation mainly takes place in the third dimension and cannot be inferred by the two-dimensional imaging of the mother drop reported herein, the relative contributions of the shear and extension to the overall deformation of the mother drop may be quantitatively assessed by the defining the nondimensional flow parameter defined implicitly via [37]

$$\nabla v = D_2 \begin{bmatrix} 0 & 1 & 0 \\ \lambda & 0 & 0 \\ 0 & 0 & 0 \end{bmatrix}. \tag{6}$$

TABLE I. Summary of the experiments. C_x stands for the xanthan concentration, Q_{i1}, Q_{i2} for the volumetric flow rates, Re_d for the drop Reynolds number, and Re for the bulk Reynolds number.

C_x (%wt)	Q_{i2} (mL/min)	Q_{i1} (mL/min)	Re_d	Re
[0, 0.2]	50	6.3	[38.8, 276]	[305, 1530]
	50	9.4	[34.7, 280]	[305, 1530]
	50	12.5	[37.1, 240]	[305, 1530]
	100	12.5	[69.3, 463]	[659, 3053]
	150	12.5	[190, 749]	[1021, 4582]

Explicitly, the flow type parameter λ may be written in terms of the second invariant of the rate of deformation tensor D_2 and the vorticity ω:

$$\lambda = \frac{D_2 - \omega}{D_2 + \omega}, \tag{7}$$

where $\omega = \partial u_y/\partial x - \partial u_x/\partial y$ is the magnitude of the vorticity.

A pure straining flow corresponds to $\lambda \to 1$ while a pure shear flow corresponds to $\lambda \to 0$. Finally, the effective strength of the straining flow may be crudely estimated as $\dot{\epsilon} \approx \lambda D_2$ and that of the shear flow as $\dot{\gamma} \approx (1 - \lambda) D_2$.

III. RESULTS

A. Summary of experiments

The experiments have been performed using as a continuous phase five distinct xanthan solutions with concentrations C_x ranging from 0% (wt) (pure water) to 0.2% (wt). For each value of the xanthan concentration five distinct pairs of flow rates at the two channel inlets have tested.

The dynamic behavior of single oil drops in the flow of the xanthan solutions is governed by an interplay between inertia, viscous effects, and capillarity [38]. It is therefore interesting to estimate the strength of each contribution for the background flows we study.

The drop Reynolds numbers are estimated according to $Re_d = \rho U_o D/(2\eta_x)$ where U_o is the mean outlet velocity and D is the initial diameter of the mother drop which ranges between [100 μm, 200 μm]. The bulk Reynolds number is defined by $Re = \rho U_{i2} H_2/\eta_x$. The viscosities of the xanthan solutions are obtained by interpolation of the rheological flow curves corresponding to the mean shear rates estimated using the flow rates, $\dot{\gamma} = 2Q_{i2}/(H_2 W_2^2)$. As one can see from the values of the bulk Reynolds number listed in Table I, the flows we study are either weakly or fully developed turbulent.

As already stated through the paper, such flows have been previously employed for producing emulsions at high throughput [35,39].

Liquid–liquid dispersion and the background flow in the microfluidic device were experimentally investigated in a broad range of flow rates [35,39]. Through these experiments the Reynolds number (estimated for the continuous aqueous phase, not by using the droplet size) was varied from 1000 to 7000 and the oil dispersed volume fraction varied between 3% and 30%. The rather large values of the Reynolds number indicate that the background flow was either weakly or fully developed turbulent. This observation has been reinforced by measurements of the pressure drops and the qualitative observation of spatially irregular clouds of dispersed droplets [39]. A more systematic space-time analysis of the background flow by means of time-resolved micro-PIV is underway and will be reported shortly in a subsequent paper.

The balance between the viscous effects and the combined inertia and capillarity is quantified by the Ohnesorge number:

$$Oh = \frac{\eta}{(\rho \sigma_i D_{av})^{1/2}}, \tag{8}$$

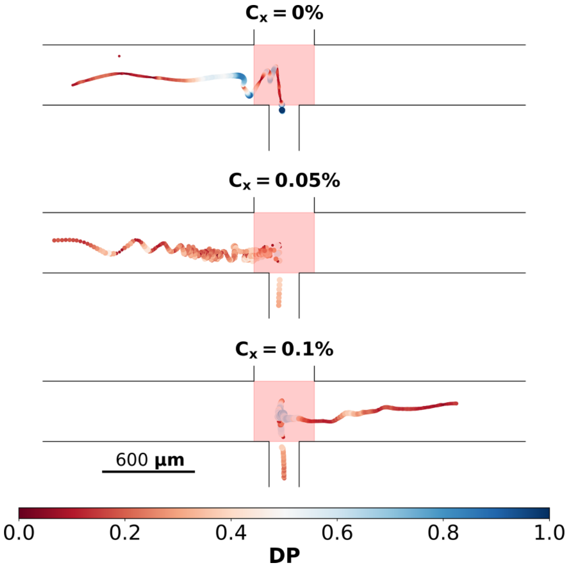

FIG. 6. Illustrations of single droplet dynamics for several xanthan concentrations indicated in the top insets and flow rates are 50–6.3 mL/min. The scatter refers to the instantaneous positions of the center of mass of the oil droplet. Both the false color and the relative size of the symbols map the deformation parameter DP. In each panel the red highlighted zone marks the impingement region.

where ρ is the density of the solutions, $\sigma_i = 21.5$ mN/m the interfacial tension, η is a scale for the viscosity, and $D_{av} = 150$ μm is the average diameter of the injected drops. As the flows we consider are driven in range of high shear rates ($\dot{\gamma} > 10^3$ s^{-1}), one may consider as a scale for the viscosity η the infinite shear viscosity η_∞ which, according to the data presented in Fig. 2(a), varies between 1.3 mPa s and 3 mPa s. With these remarks, one may conclude that through our experiments the Ohnesorge number was varied between $Oh \in [2.28 \times 10^{-2}, 5.2 \times 10^{-2}]$. The small values of the Ohnesorge number indicate that the flows are dominated by the inertia and the capillarity rather than by viscous effects.

In the presence of inertia, viscous effects and capillary forces there exist three intrinsic timescales relevant to the dynamics of the single drop. The inertio-capillary time $\tau_{ic} = (\rho D_{av}^3/\sigma_i)^{1/2}$ can be estimated $\tau_{ic} \approx 0.4$ ms. The visco-inertial time $\tau_{vi} = \rho D_{av}^2/\eta^2$ varied in between $\tau_{vi} \in [2.5\ \text{s}, 13\ \text{s}]$. Last, the Ohnesorge characteristic time $t_O = \eta^3/(\rho\sigma_i^2)$ was varied in the interval $\tau_O \in [4.74\ \text{ns}, 58.3\ \text{ns}]$.

B. Trapping and deformation dynamics of a single oil droplet for various xanthan concentrations in the continuous phase

A first aspect we focus on relates to the dynamics of trapping and deformation of single oil droplets within the impingement flow region in cases when no breakup occurs for various concentrations C_x of xanthan in the continuous phase. The effective deformation of the drop may be quantitatively described by the nondimensional deformation parameter DP initially introduced by Taylor [40]:

$$DP = \frac{L - B}{L + B}, \tag{9}$$

where L, B are the major and minor semi-axis of the drop, respectively.

The dynamics of a single oil droplet for various concentrations C_x of xanthan in the continuous phase are illustrated in Fig. 6 where successive positions of a single drop color coded by the value of the deformation parameter *DP* are plotted. As the concentration of xanthan in the continuous phase is gradually increased, the droplet spends more time within the impingement region highlighted by a red square. A clear variation of the instantaneous droplet deformation along its trajectory is noticeable in Fig. 6. For the case of pure water ($C_x = 0\%$) as a continuous phase, the droplet does not deform significantly while being trapped within the impingement region but deforms considerably after escaping this region following some sort of " *sling shot* " effect. For the shear-thinning cases we have explored ($C_x = 0.05\%,\ C_x = 0.1\%$) the droplet first deforms within the impingement region then relaxes for a short period of time while exiting the impingement region then gets deformed once more following a similar type of " *sling shot* " effect. More insights into the temporal dynamics of the droplet trapping process may be obtained by focusing on time series of the deformation parameter, their corresponding probability distributions and the average trapping times, Fig. 7.

For the case of pure water as a continuous phase, large fluctuations of the deformation parameter are observed, mostly of low frequency, Fig. 7(a). For a xanthan concentration $C_x = 0.05\%$ in the continuous phase the magnitude of fluctuations of the deformation parameter remain large but now high-frequency details are visible in the time series. For the highest xanthan concentration illustrated, the level of the high-frequency fluctuations decreases. Thus, qualitatively speaking, the time series of the deformation parameter do not seem to follow a monotonic trend with increasing concentration of xanthan in the continuous phase. This lack of a monotonic trend is, perhaps, even more visible while plotting the probability density functions of the deformation parameter *DP*, Fig. 7(b). For the case of pure water, the pdf is double peaked. For a xanthan concentration $C_x = 0.05\%$ the pdf becomes singly peaked but a further increase of the xanthan concentration $C_x = 0.1\%$ brings us back to an even more pronounced (than in the pure water case) doubly peaked shape. Yet, the trapping time t_{trapping} (defined as the time spent by the drop within the impingement region marked by a red rectangle in Fig. 6) and the time-averaged droplet deformation $\langle DP \rangle_t$ increase monotonically (basically linearly) with increasing concentration of xanthan in the continuous phase, Fig. 7(c).

In an attempt to correlate the trapping dynamics of the individual droplet and deformation with their velocity, we present in Fig. 7(d) the probability density functions (PDFs) of the in plane velocity measured for the cases illustrated in Fig. 6.

As the xanthan concentration is gradually increased no clear trend in the shape of the PDFs may be observed. This is most probably coming from the fact that the flow within the impingement region is genuinely three dimensional while, experimentally, we solely have access to a two-dimensional flow field.

It is equally instructive to monitor the probability of the droplet trapping for various xanthan concentrations in the continuous phase as a function of the flow conditions (combination of flow rates), Fig. 8(a). For the first three driving flow rates (50–6.3 mL/min, 50–9.4 mL/min, 50–12.5 mL/min) the trapping probability decreases when the xanthan concentration C_x gradually increases—the circles, squares and triangles in Fig. 8(a). For the highest flow rates investigated (100–12.5 mL/min, 150–12.5 mL/min) the trend of the probability with the xanthan concentration is reversed, see diamonds and stars in Fig. 8(a).

This *inversion* of the trend of the trapping probability with the xanthan concentration observed while switching from low to high driving flow rates indicates a significant change in the dynamics of the single droplet as the concentration of xanthan is gradually increased.

To rationalize the various single droplet dynamics observed within the impingement region in terms of the flow structure we first note that the impingement region is dominated by the presence of a three-dimensional swirling motion sketched in the bottom panel of Fig. 3(b). This swirling motion originates from the uneven sizes of the two fluid inlets, top panel of Fig. 3(b) and promotes the transition to turbulent flow states [34].

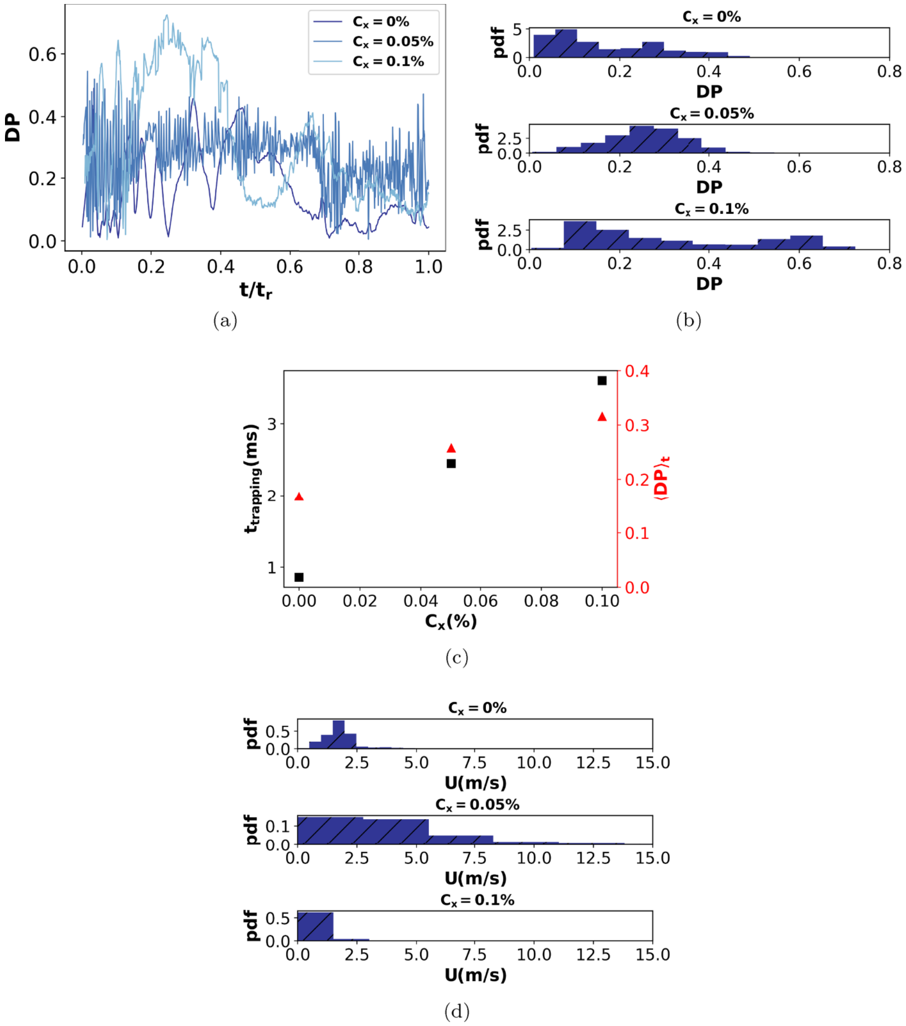

(a) (b)

(c)

(d)

FIG. 7. (a) Time series of the deformation parameter DP corresponding to the data illustrated in Fig. 6. The time axis is normalized by the residence time t_r of the drop in the field of view. (b) Probability density functions corresponding to the time series illustrated in panel (a). (c) Summary of the trapping statistics: bottom-left axis shows dependence of the trapping time t_{trapping} on the concentration of xanthan in the continuous phase, bottom-right axis shows dependence of the time-averaged deformation parameter $\langle DP \rangle_t$ on the xanthan concentration. (d) Probability density functions of the in plane velocity of an oil droplet exhibiting trapping behavior for three concentrations C_x of xanthan in the continuous phase indicated in the top insets.

In the absence of three-dimensional measurements of the flow fields within the impingement region, the effective strength of this swirling motion may be estimated as

$$\Psi_{\text{eff}} = SSI\left(\frac{\eta_w}{\eta_x}\right), \tag{10}$$

where the nondimensional swirl strength index SSI previously introduced in Ref. [35] is defined using the flow rates of the fluids fed through the inlets 1,2 of the microchannel:

$$SSI = \frac{\dot{m}_{i1}\bar{U_{i1}}^2 \frac{\bar{U_{i1}}}{\bar{U_{i1}}+\bar{U_{i2}}} d + \dot{m}_{i2}\bar{U_{i2}}^2 \frac{\bar{U_{i2}}}{\bar{U_{i1}}+\bar{U_{i2}}} d}{\dot{m}_0 \bar{U_0}^2 H}. \tag{11}$$

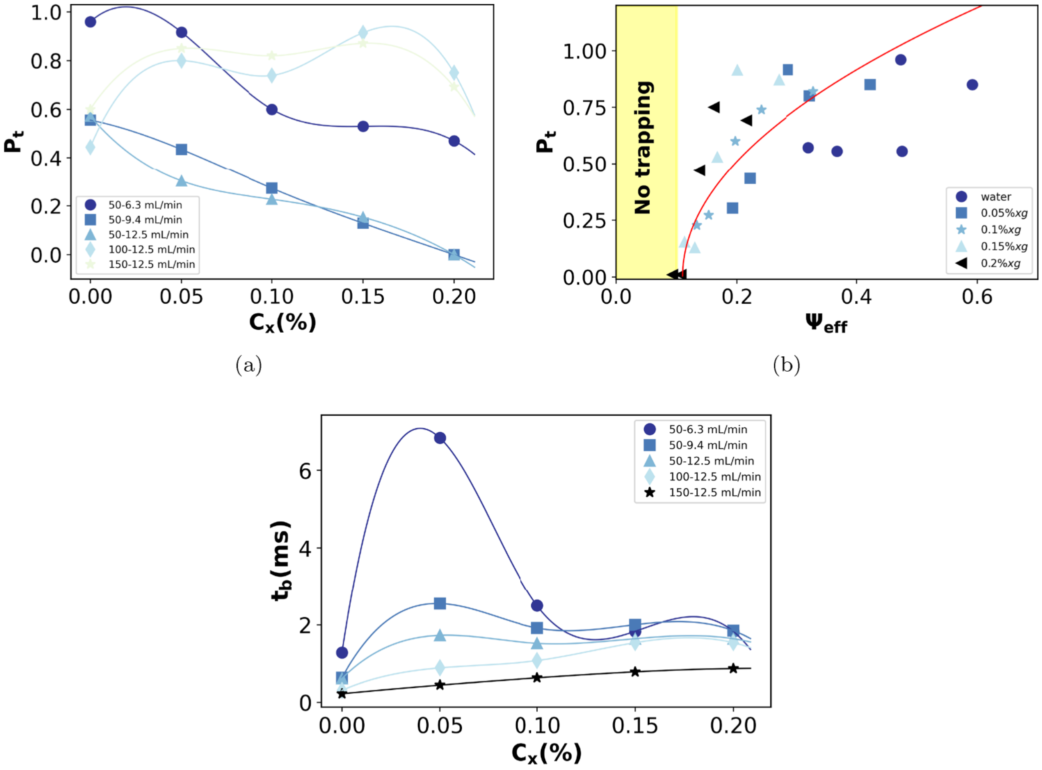

(a) (b)

(c)

FIG. 8. (a) Probability of trapping of a single oil drop as a function of the concentration C_x of xanthan in the continuous phase for several combinations of flow rates indicated in the legend. The full lines are cubic spline interpolating functions that solely serve as a guide for the eye. (b) Dependence of the trapping probability P_t on the effective swirl efficiency Ψ_{eff}. The full line is a guide for the eye, $P_t \propto (\Psi_{\text{eff}} - 0.1)^{0.5}$. (c) Dependence of the averaged (over 100 individual events) breakup times of the single oil droplet for various flow rates indicated in the inset on the volume fraction of xanthan in the continuous phase. The full lines are cubic spline interpolating functions that solely serve as a guide for the eye.

Here $\dot{m_{i1}} = \rho Q_{i1}$, $\dot{m_{i2}} = \rho Q_{i2}$ stand for the mass flow rates of the fluids injected through the inlets 1,2 of the microchannel, $\dot{m_0} = \rho Q_o$ is the flow rate measured through each of the outlets of the microchannel and $\bar{U_{i1}}$, $\bar{U_{i2}}$, $\bar{U_o}$ are the corresponding flow speeds. Here $H = H_2$ is the size of the outlets and $d = (H_2 - H_1)/2$ is the offset distance between the symmetry axis of the inlets.

The definition of the effective swirl strength in the presence of shear thinning is chosen on a rather intuitive basis so its value decreases as the viscosity η_x of the continuous phase increases (upon of a gradual increase of the xanthan concentration).

The viscosity of the xanthan solution involved in the definition of the effective swirl strength by Eq. (10) is computed via interpolation of the rheological measurements described in Sec. II A 2 and illustrated in Fig. 2(a) at values of the effective shear rate estimated using the flow rates.

The dependence of the probability for a single oil droplet of being trapped in the impingement region computed by monitoring 100 individual trapping events (droplets) on the flow parameter Ψ_{eff} is shown in Fig. 8(b). For low values of the effective flow parameter, $\Psi_{\text{eff}} \leqslant 0.1$, no droplet trapping events are observed.

When plotted against the effective swirl efficiency parameter Ψ_{eff}, the trapping probabilities measured when xanthan solutions are used as a continuous phase follow a common trend, $P_t \propto$

$(\Psi_{\mathrm{eff}} - \Psi^c_{\mathrm{eff}})^{0.5}$ with $\Psi^c_{\mathrm{eff}} \approx 0.1$ while the data acquired with water as a continuous phase fall clearly off this trend, Fig. 8(b). The square root trend observed for the xanthan data indicates that, as the effective swirl strength is gradually increased past the critical value $\Psi^c_{\mathrm{eff}} \approx 0.1$, trapping events emerge via an imperfect bifurcation.

C. Breakup dynamics of a single oil droplet for various xanthan concentrations in the continuous phase

A second interesting physical aspect relates to the dynamics of the breakup process of a single oil drop as a function of the shear-thinning rheology of the continuous phase. Understanding the breakup dynamics of a single drop is a key step towards understanding the emulsification process which is relevant to a number of applications in various engineering settings.

The physical quantity that is the most straightforward to assess is the time needed for a mother drop to undergo a primary breakup event. To assess this, we perform statistics over 100 individual mother drops tracked from the moment they entered the impingement region until until the primary breakup event occurred.

The dependence of the average breakup time t_b measured for various flow rates indicated in the top inset on the xanthan concentration C_x is shown in Fig. 8(c). The full lines are cubic spline interpolating functions that serve as a guide to visualize the trend of the data. The breakup times are closest in magnitude to the inertio-capillary timescale $\tau_{ic} \approx 0.4$ ms but separated by roughly three orders of magnitude from both the Ohnesorge timescale τ_O and the visco-inertial timescale τ_{vi}. This indicates that inertio-capillary effects control the single-drop breakup process.

Corresponding to the low flow rates explored the dependence of the breakup time on the xanthan concentration is nonmonotonic and exhibits a peak around $C_x \approx 0.05$ (the circles, squares, and triangles). As previously mentioned for other physical quantities we assessed through the paper, the location of this peak rather close to the overlap concentration C^* highlighted in Fig. 2(b). As the flow rates are gradually increased the peak flattens and, for the largest flow rates the dependence becomes monotonically increasing (the diamonds and the stars).

To get further understanding of the rather nontrivial dependence of the statistically averaged breakup times on the flow rates and xanthan concentration illustrated in Fig. 8(c), we focus in the following on a systematic description of the dynamics of the interfaces between the two fluids and the flow kinematics responsible for the drop-breakup process.

A panorama of micrographs illustrating the single droplet dynamics and breakup observed at low flow rates (50–6.3 mL/min) for various xanthan concentrations is shown in Fig. 9. The time instants are indicated in the top insets of each micrograph.

A panorama of micrographs illustrating the single droplet dynamics and breakup observed at high flow rates (150–12.5 mL/min) for various xanthan concentrations is shown in Fig. 10.

We present in Fig. 11 the time dependence of the total number of daughter droplets (or filaments) observed in the field of view. Different symbols refer to the xanthan concentrations indicated in the insets of each panel. The low speed breakup case (50–6.3 mL/min) visually illustrated in Fig. 9 is presented in Fig. 11(a) while the high-speed case visually illustrated in Fig. 10 is presented in Fig. 11(b).

At short times, the number of droplets is of order of unity. This corresponds to mainly a single large mother drop entering the impingement flow region and, occasionally, several other much smaller droplets observed in the field of view. Our analysis solely focuses on the dynamics of the mother drop. After a characteristic time t_b the initial mother droplet undergoes a primary breakup triggered by the turbulent flow field surrounding it. The characteristic time t_b for the primary breakup to occur depends on both the xanthan concentration and the flow rates which mainly control the strength of the swirling motion and, consequently, the strength of the turbulent flow. The primary breakup of the initial mother drop is followed by deformation of the resulting drops and subsequent breakup events. Consequently, for $t \geqslant t_b$, the number N_{max} of objects (daughter droplets, filaments) detected in the field of view generally increases monotonically with time expect following a power law.

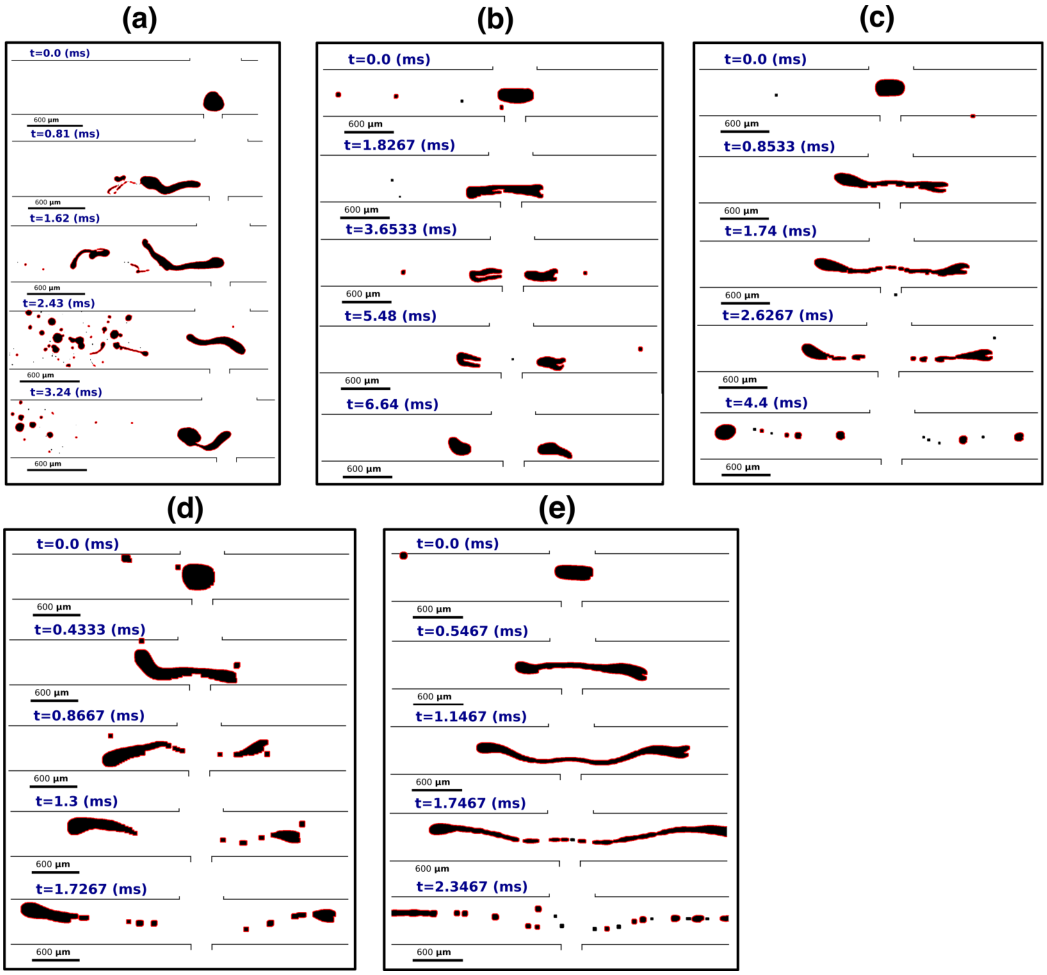

FIG. 9. Illustration of the dynamics of droplet breakup for several xanthan concentrations in the continuous phase and the flow rates 50–6.3 mL/min: (a) $C_x = 0\%$, (b) $C_x = 0.05\%$, (c) $C_x = 0.1\%$, (d) $C_x = 0.15\%$, (e) $C_x = 0.2\%$. In each panel the red contours delineate the oil-water interface.

For both flow rates investigated, the steepest increase of the number of objects is observed when water is used as a continuous phase. In the presence of xanthan, the breakup process is slower which is due to the presence of filaments.

A key element for the characterization of the dynamics of the drop-breakup process relates to a statistical analysis of the morphology of the connected objects resulting from the breakup process.

To describe the morphology of the connected objects emerging upon the breakup of the mother drop we focus on the statistics of the sphericity of the daughter droplets observed in the field of view. For each droplet, we define the nondimensional sphericity parameter

$$\xi = \frac{4\pi A}{P^2}, \tag{12}$$

where A is the area of the droplet (or filament) and P its perimeter.

This additional nondimensional parameter characterizing the droplet shape is somewhat similar to the deformation parameter DP previously defined through the paper but, as it directly involves the areas and the perimeters of the detected droplets (rather just the main semi-axis of the deformed

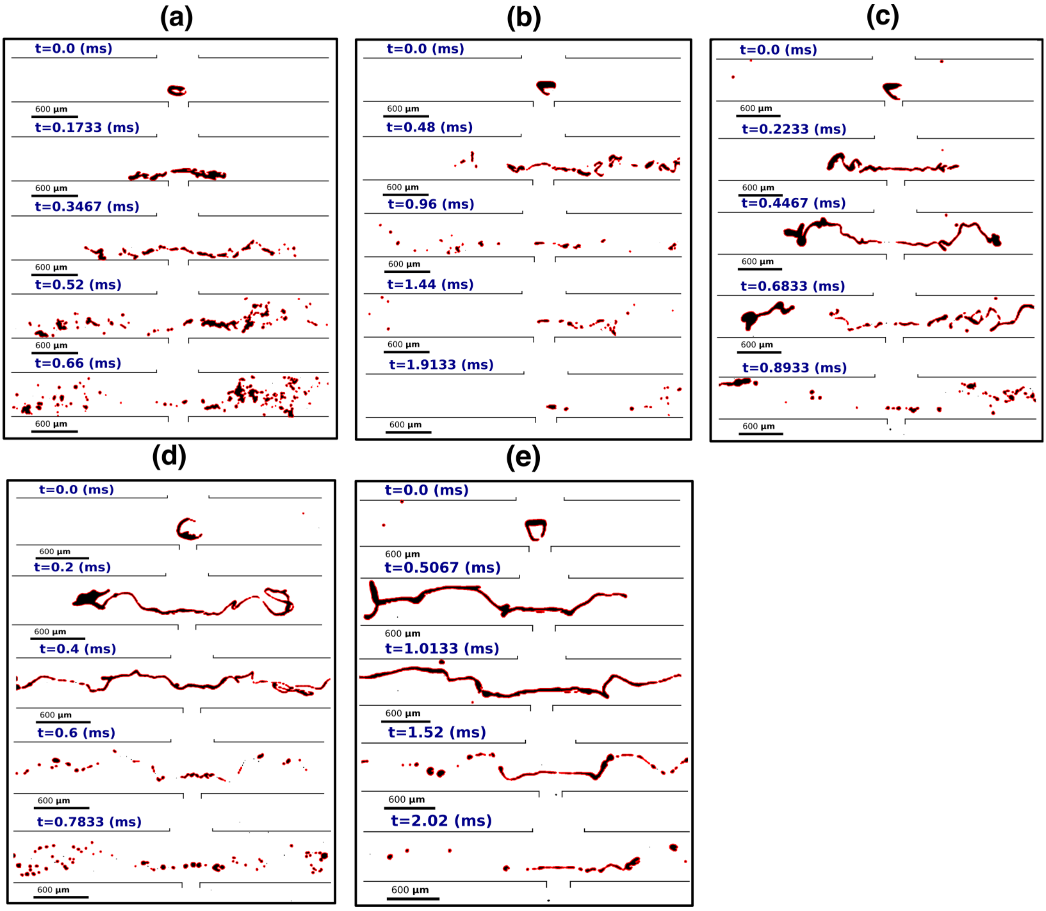

FIG. 10. Illustration of the dynamics of droplet breakup for several xanthan concentrations in the continuous phase and the flow rates 150–12.5 mL/min: (a) $C_x = 0\%$, (b) $C_x = 0.05\%$, (c) $C_x = 0.1\%$, (d) $C_x = 0.15\%$, (e) $C_x = 0.2\%$. In each panel the red contours delineate the oil-water interface.

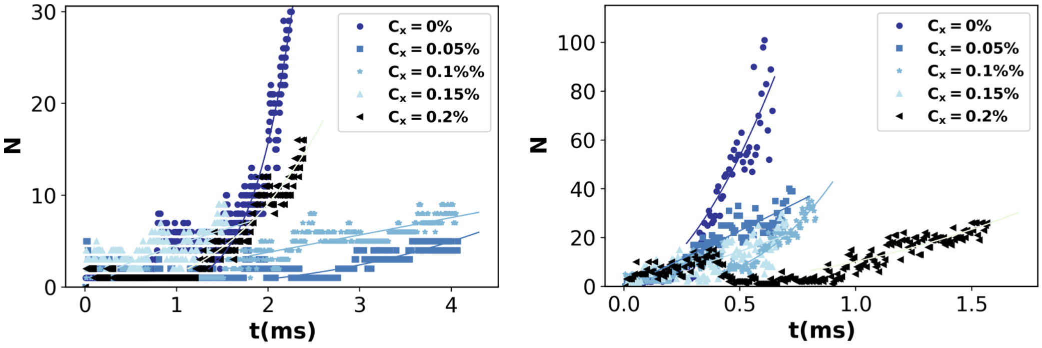

(a) (b)

FIG. 11. Temporal evolution of the number N of connected objects (daughter droplets and filaments) observed in the field of view after the breakup of the single oil droplet for various concentrations of xanthan in the continuous phase indicated in the two insets and two distinct choices of flow rates: (a) 50–6.3 mL/min and (b) 150–12.5 mL/min. The full lines in each panel are power-law fitting functions.

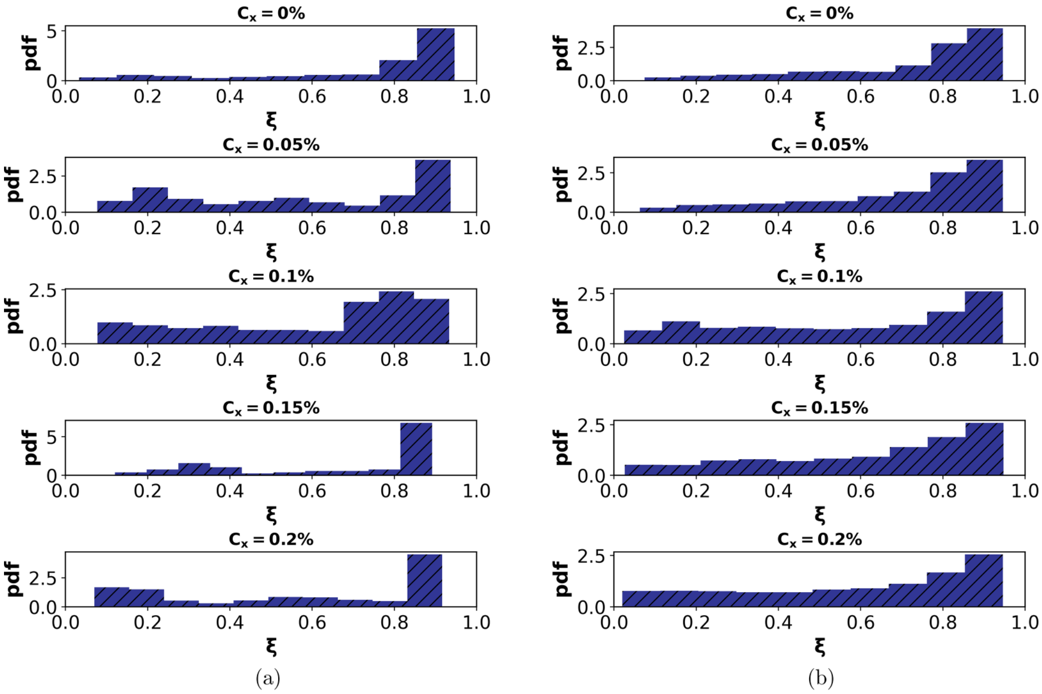

FIG. 12. Probability distributions of the sphericity parameter ξ of the oil droplets observed in the field of view for various xanthan concentrations in the continuous phase indicated in the top insets and two combinations of flow rates: (a) 50–6.3 mL/min and (b) 150–12.5 mL/min.

droplet object), it is probably more appropriate for telling the difference between quasispherical drops and filaments. Thus, for nearly spherical droplets, $\xi \rightarrow 1$ while for filament-shaped droplets that are characterized by small areas and large perimeters, $\xi \rightarrow 0$. Probability density functions (PDFs) of the sphericity parameter at various xanthan concentrations are summarized in Fig. 12.

For the low flow rates case the PDFs gradually become doubly peaked as the xanthan concentration is gradually increased, Fig. 12(a). This doubly peaked behavior of the PDFs relates to the coexistence of drops and filaments observed in Fig. 9.

A different shape and trend of the PDFs is observed for the high flow rates, Fig. 12(b). As the xanthan concentration is increased, the initial peak located near $\xi \approx 1$ related to the presence of drops broadens significantly within the region $\xi \in [0, 1]$ consistently with an increase of the number of low sphericity objects which are the long filaments observed in Fig. 10.

A key element in understanding the dynamics of the breakup phenomenon relates to assessing the flow structure around the drop. To do so, we employ the front tracking technique detailed in Sec. II C in order to assess the velocity distribution along the contour of the mother drop and, subsequently, the kinematics of its deformation. We illustrate in Fig. 13 contour speeds of an oil drop (top row) undergoing breakup in water for a combination of flow rates 50–6.3 mL/min computed at several time instants indicated in the top insets. Together with this, we illustrate on the bottom row of Fig. 13 the corresponding PDFs of the flow type parameter λ defined by Eq. (7).

Right after entering the impingement region ($t = 0.34$ ms), the drop experiences both shear and extension. At later times the extensional part of the flow increases gradually though the flow remains of mixed type. Close to the breakup ($t = 2.42$ ms) when a significant pinching effect is observed the flow field around the drop contour is extension dominated.

We illustrate in Fig. 14 time series of the total rate of deformation D_2, the extensional rate deformation $\dot{\epsilon}$ and the rate of the shear deformation $\dot{\gamma}$ computed from measurements of the contour

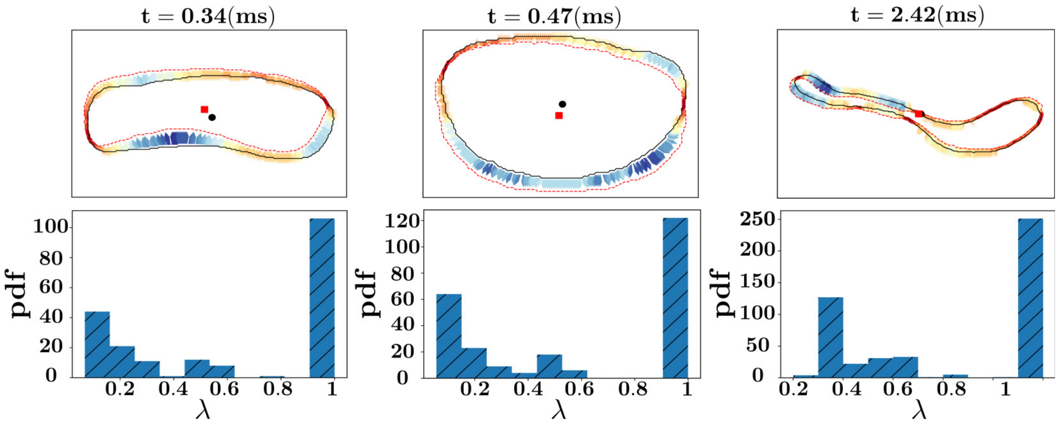

FIG. 13. Top row shows illustration of the front tracking (see Sec. II C for the technical details of the analysis) for a mother droplet in a water matrix and the flow rates 50–6.3 mL/min at several time instants indicated in the top insets. The solid black line represents the initial contour of the drop, the dashed red line is its final contour. The black circle is the initial centroid of the drop while the red square is its final centroid. The color map of the velocity vectors relates to their magnitude (red shows small values, blue shows large values). Bottom row shows corresponding probability density functions (PDFs) of the flow type parameter λ computed according to Eq. (7).

velocity field exemplified in Fig. 13. The measurements were performed with water as a continuous phase and a combination of flow rates 50–6.3 mL/min. On the top row of the plot are presented three distinct micrographs of the oil droplet corresponding to the time instants highlighted by full red circles in the main plot.

The spikes of the time series illustrated in Fig. 14 correspond to the pinch off of the mother drop which precludes a breakup event.

We present in Fig. 15 the dependence of the rates of deformation (shear: empty symbols, extension: flow symbols) averaged in time until the primary breakup occurs ($t < t_b$) on the xanthan concentration for two flow rates: 50–6.3 mL/min (circles), 150–12.5 mL/min (squares).

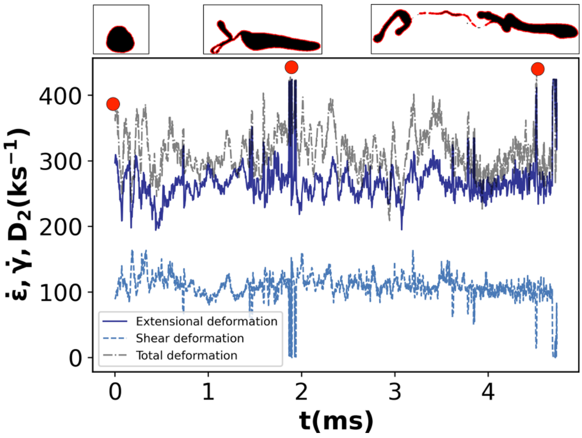

FIG. 14. Time series of the shear deformation $\dot{\gamma}$ (dashed line), extensional deformation $\dot{\epsilon}$ (full line), and total deformation D_2 (dash-dotted line). The measurements were performed with water as a continuous phase and a combination of flow rates 50–6.3 mL/min. Micrographs of the mother drop acquired at the time instants marked by the full red circles in the main plot are illustrated on the top line.

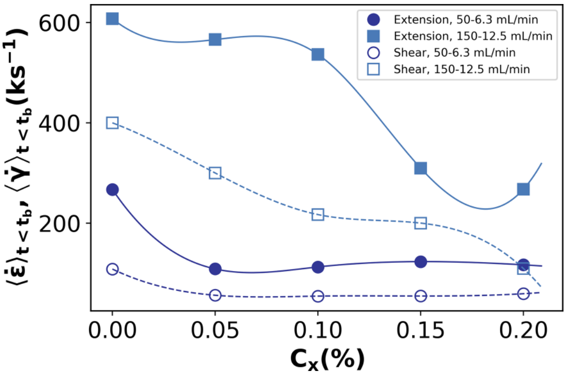

FIG. 15. Dependence of the time-averaged rates of shear (open symbols) and extension (full symbols) averaged prior to the primary breakup of the mother drop on the xanthan concentration. The symbols refer to the combinations of flow rates indicated in the inset. The lines are cubic spline interpolating functions that serve as a guide for the eye.

These measurements offer a second confirmation that the dynamics of the droplet is extension dominated and this is the case regardless the flow rates and xanthan concentrations.

It is rather clear at this point that in order to fully connect the single drop dynamics with the rheological behavior of the fluid, measurements of the extensional viscosity are needed. Unfortunately, we are not aware of any technique able to assess the extensional viscosity at such high rates of extension.

Through the reminder of the analysis we solely focus on the extensional part of the deformation field.

Based on simultaneous measurements of the time series of the characteristic size of the drop $R(t)$ (estimated using the area A and perimeter P of the drop as $R \approx 2A/P$), the speed of its centroid $V_C(t)$ and the extensional rate $\dot{\epsilon}(t)$, one can compute a time series of extensional deformations as $\epsilon(t) = R(t)\dot{\epsilon}(t)/V_C(t)$. The statistics of the extensional strains prior to the primary breakup of the mother drop ($t < t_b$) are summarized in Fig. 16 for two combinations of flow rates: 50–6.3 mL/min (circles), 150–12.5 mL/min (squares).

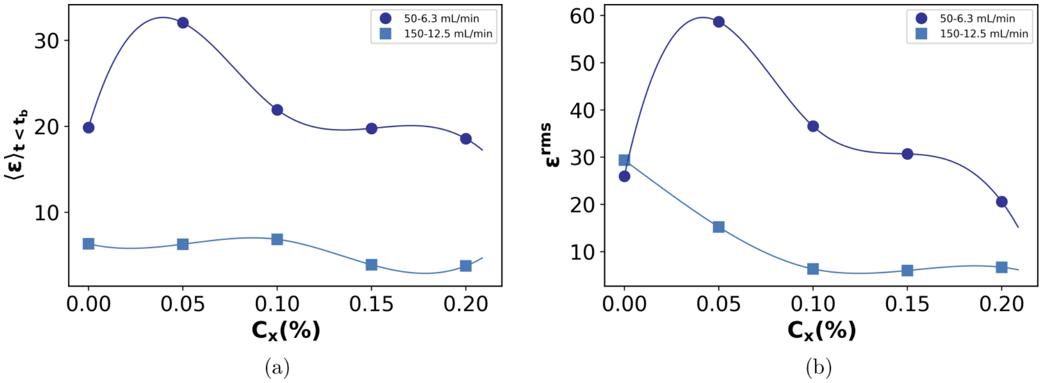

(a) (b)

FIG. 16. Statistics of the extensional strains ϵ prior to the primary breakup at various xanthan concentrations: (a) time average and (b) rms fluctuations. In each panel the symbols refer to the combinations of flow rates indicated in the inset and the lines are cubic spline interpolating functions that serve as a guide for the eye.

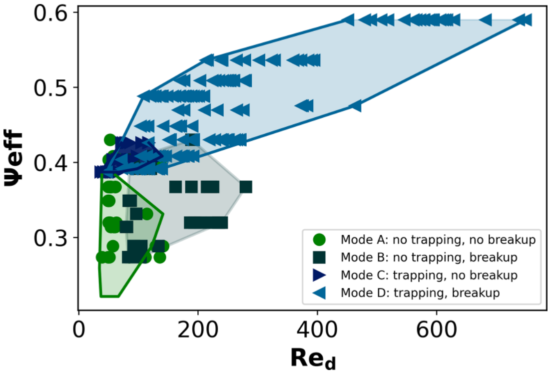

FIG. 17. Dynamic modes of single oil drop observed in both Newtonian and non-Newtonian fluid matrices. The four experimentally observed dynamic modes detailed in the paper are indicated in the legend.

For the lowest flow rates combination explored both the time-averaged rate $\langle \epsilon \rangle_{t<t_b}$ [Fig. 16(a)] and the root mean square (rms) of its fluctuations [Fig. 16(b)] are nonmonotonic in xanthan concentration and exhibit a local maximum around $C \approx C_x$. For the highest flow rates combination both the time-averaged extensional rate and the rms of its fluctuations are smaller than for the case of the smaller flow rates. It is important to note at this point that for both flow rates illustrated in Fig. 16 the rms of the fluctuations of the rate of extension is typically larger than its time-averaged value which is consistent with the large values of the Reynolds number that render the primary swirling flow in the impingement region strongly turbulent.

We summarize in Fig. 17 the various dynamic modes of a single oil droplet observed for various xanthan concentrations and various combinations of flow rates as a function of the effective swirl efficiency parameter Ψ_{eff} and the Reynolds number. The two fundamental dynamic modes discussed in Secs. III B and III C are mode C (trapping, no breakup, right triangles) and mode B (no trapping, breakup, squares). By exploring a wide range of flow rates and several xanthan concentrations, two additional dynamic modes that are combinations of the first two are observed: mode A (no trapping, no breakup, circles) and mode D (trapping, breakup, left triangles). Corresponding to low values of the Reynolds numbers, only the modes A and C are observed. Upon a gradual increase of the Reynolds number and of the swirl efficiency parameter, modes B and D start to develop. Corresponding to the highest values of the Reynolds number explored, only mode D is observed.

IV. CONCLUSIONS, OUTLOOK

A systematic experimental investigation of the dynamics of a Newtonian droplet (oil) in the turbulent cross-slot flow of xanthan solutions with various concentrations is presented.

The key physical processes underlying the emulsification in turbulent flow are the transient droplet deformation and, ultimately, its breakup. The present study brings insights into the role of shear-thinning rheological behavior on each of these two processes which may prove instrumental in understanding the dynamically more complex process of emulsification of shear-thinning fluids in turbulent flows.

Two distinct phenomena have been studied by means of *in situ* visualization and a bespoke image processing protocol developed in house. The first one relates to the trapping of the mother droplet within the impingement region of the flow in the absence of breakup, Sec. III B. The swirl generated by the uneven sizes of the flow inlets within the impingement region translates into low pressures within the impingement region which lead to the drop trapping phenomenon.

Within these states the droplet does deform to a certain extent both while being trapped in the impingement zone and after escaping it but it does not breakup. Both the trajectories and the histories of their deformation depend on the concentration of xanthan in the continuous phase, Fig. 6. The main statistics of the trapping events are summarized in Fig. 7 in terms of both the drop deformation parameter DP and trapping time t_{trapping} for several concentrations of xanthan in the continuous phase. The central result relates to a monotonic increase of the trapping time when the xanthan concentration is gradually increased. Together with this, the longer the drops stay trapped, the larger is their time-averaged deformation $\langle DP\rangle_t$. The statistics of the drop velocity do not follow a clear trend with the xanthan concentration, Fig. 7(d). Although we do not have a definite explanation for this we believe it may originate from either the three dimensionality of the flow (we only have access to the in-plain velocity) or the coupling between the flow kinematics and the shear-thinning rheology of the continuous phase. The trend of the dependence of the trapping probability P_t with the xanthan is strongly influenced by the magnitude of the driving flow rates, Fig. 8(a). For low values of the flow rates, the trapping probability decreases monotonically with the xanthan concentration; while for higher flow rates the dependence becomes nonmonotonic. This is a clear indicator that the trapping behavior relates to both the flow conditions (the flow rates) and the shear-thinning rheology of the continuous phase. This prompted us to define a nondimensional parameter Ψ_{eff} that quantifies the effective strength of the swirling motion that dominates the impingement region by accounting for both the inlet flow conditions (flow rates) and the rheological behavior, Eq. (10). Indeed, when plotted against the this effective flow strength parameter, the trapping probabilities follow a common square root trend indicating that with respect to this control parameter the trapping events emerge via an imperfect bifurcation, Fig. 8(b).

A second phenomenon that is of paramount importance for understanding the process of emulsification relates to the breakup of drops, Sec. III C. The characteristic breakup times depend on both the flow rates and the rheology of the continuous phase, Fig. 8(c). For low flow rates, the dependence of the breakup time on the xanthan concentration is nonmonotonic exhibiting a peak around the overlap concentration C^*. For higher flow rates a monotonic dependency of the breakup time on the xanthan concentration is observed: the larger the concentration is, the longer it takes for the mother drop to break. The intricate coupling between the breakup dynamics, flow conditions and rheology of the continuous phase prompted us to resort to a systematic analysis of the drop morphology, Figs. 9 and 10. The breakup of the mother drops yields two morphological distinct connected objects: daughter drops and filaments.

The time dependence of the number of connected objects observed in the field of view is summarized in Fig. 11 for two combinations of flow rates and several xanthan concentrations in the continuous phase. After the primary breakup of the mother drop, the number of connected objects increases as a power law in time. The rate of this increase depends on both the flow rates and the concentration of xanthan. For both combinations of flow rates illustrated in Fig. 11 the steepest increase of the number of connected objects is observed when pure water is used as a continuous phase. As the concentration of xanthan is gradually increased, the rate of increase of number of connected objects decreases indicating that the shear-thinning rheology of the continuous phase inhibits the dynamics of the successive breakup events.

To distinguish between the connected objects emerging upon the breakup of a mother drop and provide a statistical picture of their emergence, we have computed for each object detected in the field of view a sphericity parameter ξ defined by Eq. (12). The statistics of the sphericity parameter are summarized in Fig. 12 for two combinations of flow rates and various concentrations of xanthan in the continuous phase. In the absence of xanthan in the continuous phase, the PDFs of the sphericity are peaked at large values, $\xi \approx 0.85$ indicated that the drops represent the dominant morphology. At smaller flow rates, a gradual increase of the xanthan concentration renders the PDFs of the sphericity doubly peaked, Fig. 12(a). This corresponds to a coexistence of drops and filaments as visible in Fig. 9. The shape of the PDFs is substantially different at higher flow rates, Fig. 12(b). Upon an increase of the xanthan concentration the PDFs remain single peaked but a low ξ tail gradually develops indicating the progressive emergence of filaments which become now significantly long, Fig. 10.

Key insights into the breakup dynamics of a single drop entering the impingement region of the microchannel may be obtained by a systematic description of the flow kinematics. Such description is classically achieved using the particle image velocimetry technique, which cannot be technically implemented here. Alternatively, a simple yet novel technique is proposed that allows one to compute the distribution of the velocity along the contour of the drop, Figs. 5(b) and 13. The measurements of the contour velocity allows one to compute the second invariant of the rate of deformation tensor D_2 according to Eq. (5). To distinguish between the shear and extensional part of the drop deformation, we subsequently compute the flow-type parameter λ according to Eq. (7). An important conclusion drawn from the measurements of the flow parameter is that the deformation of the drop encompasses both shear and extension—see bottom row in Fig. 13. In terms of the magnitude of the rates of the deformation, however, the extension appears to be dominant, Fig. 14. At high flow rates, the averaged rates of deformation are more sensitive to the xanthan concentration (and follow a decreasing trend) than at low flow rates, Fig. 15. The breakup process of the droplet depends on both the average rates of extension (or the capillary number) and the average deformation. This prompted us to perform a statistical analysis of the extensional deformations, Fig. 16. For the lowest combination of flow rates investigated, the extensional deformations averaged in time until the primary breakup of mother drop was observed to follow a nonmonotonic trend with the xanthan concentration which passes through a local maximum around $C \approx C^*$, the circles Fig. 16(a). This nonmonotonic dependence is very similar in shape with the dependence of the breakup times on the concentration, Fig. 8(c). For the highest combination of the flow rates explored, the averaged strains are less sensitive to the xanthan concentration, the squares in Fig. 16(a). Quite interestingly, the averaged values of the extensional strains measured at high flow rates are smaller than those measured at lower flow rates. The turbulent microscopic flow that leads to the successive breakup events is characterized by strong fluctuations of both the rates of deformation, Fig. 14, and of the time-averaged extensional strains, Fig. 16(b). The dynamic modes associated with the droplet trapping and breakup depend on both the values of the effective swirl parameter Ψ_{eff} and the Reynolds number of the mother drop, Fig. 17.

The relevance of the present study is twofold. First, along a fundamental line, our this study provides valuable insights into the role of shear-thinning rheological behavior on both the transient deformation of droplets and their subsequent breakup in a turbulent flow. As already stated through the paper, we believe these insights might prove instrumental in understanding the dynamically more complex problem of microscopic scale emulsification.

Along a more applied and technical line, our study proposes a novel state of art technique of assessing the flow fields along the contour of the drops based on a front tracking algorithm. This method which complements the classical micro-*PIV* technique is rather straightforward to implement as it solely requires sharp images of the drops and ultimately provides a full kinematic description of the flow field responsible for the droplet deformation and its subsequent breakup.

Our experimental observations prompt for several aspects to be dealt with in future studies. First, it would be interesting to implement microscopic *PIV* measurements and quantitatively assess the space-time dynamics of the flow fields. Our study has clearly demonstrated that the primary breakup of the oil drop is mainly driven by the strong extensional component, Figs. 14 and 15. As it would be interesting at this point to understand the scaling of the critical capillary number at breakup (defined using a scale for the rates of extension) with the control parameter Ψ_{eff}, reliable measurements of the extensional viscosity are needed. This calls for new developments in extensional rheology at rates comparable in magnitude to those we report.

ACKNOWLEDGMENT

We gratefully acknowledge the “Region Pays de la Loire” for funding the project *Connect Talent ODE “Optical Diagnostics for Energy.”*

[1] L. D. Landau and E. M. Lifshitz, *Statistical Physics, Part 1: Volume 5 (Course of Theoretical Physics)*, 3rd ed. (Butterworth-Heinemann, Oxford, 1980).
[2] Herbert Callen, *Thermodynamics and an Introduction to Thermostatistics* (Wiley, New York, 1985).
[3] P. K. Kilpatrick, Water-in-crude oil emulsion stabilization: Review and unanswered questions, Energy Fuels **26**, 4017 (2012).
[4] T. Burghelea and V. Bertola, *Transport Phenomena in Complex Fluids* (Springer International Publishing, 2019).
[5] C.-X. Zhao and A. P. J. Middelberg, Two-phase microfluidic flows, Chem. Eng. Sci. **66**, 1394 (2011).
[6] S. Guido, M. Simeone, and F. Greco, Effects of matrix viscoelasticity on drop deformation in dilute polymer blends under slow shear flow, Polymer **44**, 467 (2003).
[7] D. C. Tretheway and L. G. Leal, Deformation and relaxation of newtonian drops in planar extensional flows of a Boger fluid, J. Non-Newtonian Fluid Mech. **99**, 81 (2001).
[8] L. Derzsi, M. Kasprzyk, J. P. Plog, and P. Garstecki, Flow focusing with viscoelastic liquids, Phys. Fluids **25**, 092001 (2013).
[9] M. Nooranidoost, D. Izbassarov, and M. Muradoglu, Droplet formation in a flow focusing configuration: Effects of viscoelasticity, Phys. Fluids **28**, 123102 (2016).
[10] A. Gupta and M. Sbragaglia, A lattice Boltzmann study of the effects of viscoelasticity on droplet formation in microfluidic cross-junctions, Eur. Phys. J. E: Soft Matter Biol. Phys. **39**, 2 (2016).
[11] Y. Ren, Z. Liu, and H. C. Shum, Breakup dynamics and dripping-to-jetting transition in a newtonian/shear-thinning multiphase microsystem, Lab Chip **15**, 121 (2015).
[12] A. A. Fragkopoulos, E. Pairam, L. Marinkovic, and A. Fernández-Nieves, Breakup dynamics of toroidal droplets in shear-thinning fluids, Phys. Rev. E **97**, 021101(R) (2018).
[13] T. Fu, Y. Ma, and H. Z. Li, Breakup dynamics of slender droplet formation in shear-thinning fluids in flow-focusing devices, Chem. Eng. Sci. **144**, 75 (2016).
[14] H. Zhou, C. Zhu, T. Fu, Y. Ma, and H. Z. Li, Dynamics and interfacial evolution for bubble breakup in shear-thinning non-Newtonian fluid in microfluidic T-junction, Chem. Eng. Sci. **208**, 115158 (2019).
[15] E. Chiarello, L. Derzsi, M. Pierno, G. Mistura, and E. Piccin, Generation of oil droplets in a non-Newtonian liquid using a microfluidic T-junction, Micromachines **6**, 1825 (2015).
[16] E. Chiarello, A. Gupta, G. Mistura, M. Sbragaglia, and M. Pierno, Droplet breakup driven by shear thinning solutions in a microfluidic T-junction, Phys. Rev. Fluids **2**, 123602 (2017).
[17] V. G. Agarwal, R. Singh, S. S. Bahga, and A. Gupta, Dynamics of droplet formation and flow regime transition in a T-shaped microfluidic device with a shear-thinning continuous phase, Phys. Rev. Fluids **5**, 044203 (2020).
[18] R. Nehme, W. Blel, A. Montillet, J. Bellettre, and L. Marchal, Production of oil in water emulsions in microchannels at high throughput: Evaluation of emulsions in view of cosmetic, nutraceutical or pharmaceutical applications, Chem. Eng. Process. **161**, 108301 (2021).
[19] G. Sworn, *Handbook of Hydrocolloids* (CRC Press, Boca Raton, 2009), Chap. 8, pp. 186–203.
[20] A. Roy, Synthèse et caractérisation de dérivés amphiphiles du xanthane, Ph.D. thesis, Le Havre University, 2015, https://theses.hal.science/tel-01666127/document.
[21] G. Van Aken, *Food Polysaccharides and Their Applications,* 2nd ed. (CRC Press, Taylor & Francis, Boca Raton, 2009), Chap. 15, pp. 521–539.
[22] A. B. Rodd, D. E. Dunstan, and D. V. Boger, Characterisation of xanthan gum solutions using dynamic light scattering and rheology, Carbohydr. Polym. **42**, 159 (2000).
[23] D. J. McClements, *Food Emulsions: Principles, Practices, and Techniques*, 2nd ed. (CRC Press, Boca Raton, 2005), p. 609.
[24] C. J. Pipe, T. S. Majmudar, and G. H. McKinley, High shear rate viscometry, Rheol. Acta **47**, 621 (2008).
[25] J. Sepulveda, A. Montillet, D. D. Valle, T. Amiar, H. Ranchon, C. Loisel, and A. Riaublanc, Experimental determination and modeling of flow curves of xanthan gum solutions over a large range of shear rates, Appl. Rheol. **31**, 24 (2021).
[26] P. Guillot, P. Panizza, J.-B. Salmon, M. Joanicot, A. Colin, C.-H. Bruneau, and T. Colin, Viscosimeter on a microfluidic chip, Langmuir **22**, 6438 (2006).

[27] P. Nghe, E. Terriac, M. Schneider, Z. Z. Li, M. Cloitre, B. Abecassis, and P. Tabeling, Microfluidics and complex fluids, Lab Chip **11**, 788 (2011).

[28] C. W. Macosko, *Rheology: Principles, Measurements, and Applications* (Wiley, New York, 1994).

[29] C. Miller, Predicting non-Newtonian flow behavior in ducts of unusual cross section, Ind. Eng. Chem. Fundam. **11**, 524 (1972).

[30] E. M. Nsengiyumva and P. Alexandridis, Xanthan gum in aqueous solutions: Fundamentals and applications, Int. J. Biol. Macromol. **216**, 583 (2022).

[31] A. Montillet, S. Nedjar, and M. Tazerout, Continuous production of water-in-oil emulsion using micromixers, Fuel **106**, 410 (2013).

[32] R. Lopes, R. O. Rodrigues, D. Pinho, V. Garcia, H. Schütte, R. Lima, and S. Gassmann, Low cost microfluidic device for partial cell separation: Micromilling approach, in *2015 IEEE International Conference on Industrial Technology (ICIT)* (Institute of Electrical and Electronics Engineers, Manhattan, NY, 2015), pp. 3347–3350.

[33] T. Thorsen, S. J. Maerkl, and S. R. Quake, Microfluidic large-scale integration, Science **298**, 580 (2002).

[34] A. Belkadi, D. Tarlet, A. Montillet, J. Bellettre, and P. Massoli, Water-in-oil emulsification in a microfluidic impinging flow at high capillary numbers, Int. J. Multiphase Flow **72**, 11 (2015).

[35] Y. Ji, J. Bellettre, A. Montillet, and P. Massoli, Experimental investigation on single drop breakage in two-stream impinging microchannels, Exp. Fluids **62**, 17 (2021).

[36] S. van der Walt, J. L. Schönberger, J. Nunez-Iglesias, F. Boulogne, J. D. Warner, N. Yager, E. Gouillart, T. Yu, and the scikit-image contributors, Scikit-image: Image processing in Python, PeerJ **2**, e453 (2014).

[37] G. G. Fuller and L. G. Leal, The effects of conformation-dependent friction and internal viscosity on the dynamics of the nonlinear dumbbell model for a dilute polymer solution, J. Non-Newtonian Fluid Mech. **8**, 271 (1981).

[38] M. A. Fardin, M. Hautefeuille, and V. Sharma, Spreading, pinching, and coalescence: The ohnesorge units, Soft Matter **18**, 3291 (2022).

[39] Y. Ji, J. Bellettre, A. Montillet, and P. Massoli, Fast oil-in-water emulsification in microchannel using head-on impinging configuration: Effect of swirl motion, Int. J. Multiphase Flow **131**, 103402 (2020).

[40] G. I. Taylor, The formation of emulsions in definable fields of flow, Proc. R. Soc. London, Ser. A **146**, 501 (1934).